Stability of plane Poiseuille–Couette flows of a piezo-viscous fluid

Thien Duc Tran [a] and Sergey A. Suslov [b,*]

[a] *Computational Engineering and Science Research Centre, University of Southern Queensland, Toowoomba, Queensland 4350, Australia*

[b] *Department of Mathematics and Computing and Computational Engineering and Science Research Centre, University of Southern Queensland, Toowoomba, Queensland 4350, Australia*

Abstract

We examine stability of fully developed isothermal unidirectional plane Poiseuille–Couette flows of an incompressible fluid whose viscosity depends linearly on the pressure as previously considered in [1,2]. Stability results for a piezo-viscous fluid are compared with those for a Newtonian fluid with constant viscosity. We show that piezo-viscous effects generally lead to stabilisation of a primary flow when the applied pressure gradient is increased. We also show that the flow becomes less stable as the pressure and therefore the fluid viscosity decrease downstream. These features drastically distinguish flows of a piezo-viscous fluid from those of its constant-viscosity counterpart. At the same time the increase in the boundary velocity results in a flow stabilisation which is similar to that observed in Newtonian fluids with constant viscosity.

Key words: pressure-dependent viscosity, piezo-viscous fluid, plane Poiseuille–Couette flow, hydrodynamic stability

1 Introduction

Piezo-viscous fluids (PVF) form an interesting non-Newtonian class. Polymer melts [3], lubricating oil in journal bearings [4,5] and magma in the Earth core are just a few examples of such fluids. In their flows, the shear stress (and effective viscosity) increases with the increasing normal stress. The properties

* Corresponding author
Email address: ssuslov@usq.edu.au (Sergey A. Suslov).

of piezo-viscous fluids were studied by a number of authors over the past two decades [6–8, e.g.]. The simplest rheological model which accounts for such a behaviour assumes that the viscosity of a fluid is proportional to the pressure. Perhaps the most comprehensive cycle of recent works studying this model both mathematically and numerically is by Hron, Málek, Rajagopal and collaborators [1,9–13]. The major goals of the analysis presented in this paper are to expose the physical mechanism of flow instability in such fluids and to shed more light onto the existence of simple parallel flows of piezo-viscous fluids.

Simple steady plane parallel flows of piezo-viscous shear-independent and shear-thinning fluids were first considered in [1]. In a later work [14] it was shown that simple parallel piezo-viscous flows can only exist if the viscosity is a linear function of pressure. Therefore this rheological model will be used in the current work. Our previous study [2] of such a model showed that shear-thinning effects do not lead to any qualitative changes in simple flow structure in comparison with the solutions obtained for shear-independent fluids. Yet piezo-viscous effects result in completely new flow features such as choking of the pressure-driven flow and the existence of a limiting linear velocity profile for high-speed Couette flow of piezo-viscous fluid. Therefore the current work is fully focused on the conceptual investigation of piezo-viscous effects on the stability of Poiseuille–Couette flow of a fluid with shear-independent viscosity. This will enable us to compare our results directly with the well-known stability findings for Couette–Poiseuille flows of conventional Newtonian fluids with pressure-independent viscosity (for brevity we will refer to such fluids as NF in this paper) investigated previously [15–18]. We will report at least two new features (flow stabilisation with increasing pressure gradient and a downstream flow destabilization) which are not observed in conventional NF flows. We will also show that similarly to NF flows PVF Couette flow remains stable with respect to infinitesimal disturbances so that the transition to instability is detected only for mixed Poiseuille–Couette flows with a non-zero pressure gradient applied along the channel.

To achieve the set goal in the most straightforward way two major simplifications are introduced. Firstly, note that in contrast to ordinary fluids, the viscosity of PVF necessarily changes along the channel since the applied pressure gradient driving the flow leads to pressure reduction in the downstream direction. We will assume in our analysis and then confirm numerically that such a variation is sufficiently slow and occurs on a much longer length scale than the characteristic disturbance wavelength. This enables us to apply a standard normal mode expansion in which the actual location along the channel enters as a parameter. Such an approach will be discussed in detail in Section 4. Secondly, we consider only small two-dimensional disturbances. For NF flows this is warranted by Squire's theorem which states that two-dimensional perturbations are the most dangerous (see, for example, [19]). However Squire's

theorem cannot be proven for PVF flows in which fluid viscosity changes in the streamwise direction. Yet if such a change occurs slowly, it can be shown that Squire's theorem holds locally. In order not to distract the reader from the main focus of the article and to keep the manuscript reasonably short we leave the detailed discussion of this aspect outside the scope of this paper. We also note that full three-dimensional treatment of the problem does not change any of the conclusions regarding the physical nature of instabilities drawn using a simplified two-dimensional approach. Therefore two-dimensional treatment is fully adequate for our goal of a conceptual analysis.

2 Problem definition and governing equations

Consider the flow of an incompressible fluid with pressure-dependent viscosity between two parallel horizontal plates separated by the distance $2L$ from each other. The top plate moves with velocity V^* from left to right, the bottom plate is stationary. The pressure gradient $\nabla\pi$ is applied along the channel which (depending on its direction) can either enhance or partially suppress the fluid flow caused by the motion of the upper wall. The flow is described by the equations first given in [1] which, in the case of shear-independent fluid, become

$$\rho\frac{d\mathbf{u}}{dt} = -\nabla\pi + \nabla\cdot(2\mu(\pi)|\mathbf{D}) \,, \tag{1}$$

$$\nabla\cdot\mathbf{u} = 0 \,, \tag{2}$$

where we neglect the gravity and assume that the velocity field $\mathbf{u}$ is two-dimensional with components (u, v) in the (x, y) directions, respectively. We choose the coordinate system in such a way that the x and y axes have positive right and upward directions, respectively, and the horizontal centre-plane of a channel is located at $y = 0$. In equation (1),

$$\mathbf{D} = \frac{1}{2}\begin{bmatrix} 2\frac{\partial u}{\partial x} & \frac{\partial u}{\partial y}+\frac{\partial v}{\partial x} \\ \frac{\partial u}{\partial y}+\frac{\partial v}{\partial x} & 2\frac{\partial v}{\partial y} \end{bmatrix} . \tag{3}$$

Governing equations (1)–(3) are complemented by the constitutive relations

$$\rho = \text{const.} \,, \quad \mu = a\pi > 0 \tag{4}$$

and the no-slip/no-penetration boundary conditions

$$(u, v) = (0, 0) \text{ at } y = -L \quad \text{and} \quad (u, v) = (V^*, 0) \text{ at } y = L \,. \tag{5}$$

We non-dimensionalise the equations using L, pressure π^* evaluated at $(x,y)=(0,0)$, $u^*=(\pi^*/\rho)^{1/2}$ and $t^*=L(\rho/\pi^*)^{1/2}$ as the scales for length, pressure, velocity and time, respectively, to obtain

$$\frac{\partial \mathbf{u}}{\partial t}+(\mathbf{u}\cdot\nabla)\mathbf{u}=-\nabla\pi+\alpha\nabla\cdot(2\pi\mathbf{D})\,, \tag{6}$$

$$\nabla\cdot\mathbf{u}=0\,, \tag{7}$$

$$(u,v)=(0,0)\text{ at }y=-1\quad\text{and}\quad(u,v)=(V,0)\text{ at }y=1\,, \tag{8}$$

$$\pi=1\quad\text{at}\quad(x,y)=(0,0)\,, \tag{9}$$

where $V=V^*(\rho/\pi^*)^{1/2}$,

$$\alpha=a\left(\frac{\pi^*}{\rho L^2}\right)^{1/2} \tag{10}$$

and all symbols now denote the corresponding non-dimensional quantities.

3 Basic flow

Equations (6)–(9) admit a steady parallel flow solution $\mathbf{u}=(U(y),0)$, $\pi=\Pi(x,y)$ discussed in detail in [1,2]. As will be shown in Section 5 such a flow becomes unstable when the applied pressure gradient is sufficiently strong and the wall velocity is relatively small. We refer to such flows as Poiseuille-type or Poiseuille–Couette flows. They are characterised by the existence of an extremum point $-1\le Y\le 1$ of the velocity profile such that $U'\gtrless 0$ for $y\lessgtr Y$. In this case the solution is given by (see [1,2])

$$U(y)=\begin{cases}\int_{-1}^{y}\frac{1}{\alpha}\frac{e^{C_0(s-Y)}-1}{e^{C_0(s-Y)}+1}\,ds\,, & -1\le y\le Y\,,\\ V+\int_{y}^{1}\frac{1}{\alpha}\frac{1-e^{C_0(s-Y)}}{1+e^{C_0(s-Y)}}\,ds\,, & Y\le y\le 1\,,\end{cases} \tag{11}$$

$$\Pi(x,y)=\frac{1+e^{C_0(Y-y)}}{1+e^{C_0Y}}e^{C_0(x+y)/2}\,. \tag{12}$$

The extremum point Y is determined using the velocity continuity condition $U(Y_{+0})=U(Y_{-0})$.

The integration of (11) leads to

$$U(y)=\frac{1-y+2Y}{\alpha}+\frac{2}{\alpha C_0}\ln\frac{e^{C_0(y-Y)}+1}{e^{C_0(1+Y)}+1}\,,\quad Y=\frac{1}{C_0}\ln\frac{e^{C_0}-e^{\frac{\alpha VC_0}{2}}}{e^{C_0+\frac{\alpha VC_0}{2}}-1}\,. \tag{13}$$

The stability investigation of this family of simple flow solutions is the major goal of the current study. For pure Poiseuille flow ($V=0$) equation (13)

reduces to $Y = 0$ and

$$U(y) = \frac{1-y}{\alpha} + \frac{2}{\alpha C_0} \ln \frac{1+e^{C_0 y}}{1+e^{C_0}} \equiv \frac{2}{\alpha C_0} \ln \frac{\cosh(C_0 y/2)}{\cosh C_0/2} \tag{14}$$

which was originally derived in [1]. In the limit $(C_0, V) \to (0,0)$ expressions (12) and (13) become

$$U(y) \approx \frac{1+y}{2} V + \frac{C_0}{4\alpha}(y^2-1)\left(1 - \frac{V^2\alpha^2}{4}\right), \tag{15}$$

$$\Pi(x,y) \approx 1 + \left(x + \frac{V\alpha y}{2}\right)\frac{C_0}{2} + \left(x^2 + y^2 + \alpha V x y\right)\frac{C_0^2}{8}, \tag{16}$$

The exact expressions for NF Poiseuille–Couette flow are

$$U(y) = \frac{1+y}{2} V + \frac{C_0}{4\alpha}(y^2-1), \quad \Pi(x) = 1 + \frac{C_0}{2} x. \tag{17}$$

The comparison of expressions (15)–(17) shows that in the limit $(C_0, V) \to (0,0)$ the PVF and NF flows become identical and parameter C_0 essentially characterises the applied longitudinal pressure gradient. Without loss of generality we assume that it is negative so that the fluid is encouraged to flow in the direction of increasing x. Also note that the quantity $4\alpha V/|C_0|$ is the ratio of the wall velocity and the maximum velocity of the Poiseuille component of the flow. This quantity will be conveniently used to characterise the shape of the basic flow velocity profile in the subsequent discussion. If $\alpha V/|C_0| \geq 1$ then the velocity profile becomes monotonic. We refer to such a flow as Couette–Poiseuille flows. However we will show that instability is possible only when $\alpha V/|C_0| < 1$. We call such flows Poiseuille–Couette flows. For a more straightforward comparison with conventionally non-dimensionalised NF solutions we also define Reynolds number Re^* using (10):

$$Re^* = \frac{\rho U|_{y=0} u^* L}{\mu^*} = \frac{\rho u^* L}{\mu^*}\left(\frac{V}{2} - \frac{C_0}{4\alpha}\right) = \left(\frac{V}{2} - \frac{C_0}{4\alpha}\right)\frac{1}{\alpha}. \tag{18}$$

We will use it instead of α in the subsequent discussion.

4 Linearised perturbation equations

Next we investigate linear stability of the basic states discussed in Section 3 with respect to small-amplitude velocity and pressure disturbances $\mathbf{u_1} = (u_1, v_1)$ and π_1, respectively. The linearisation about a parallel basic flow leads to the following perturbation equations

$$\frac{\partial u_1}{\partial t}+U\frac{\partial u_1}{\partial x}+v_1U'=-\frac{\partial \pi_1}{\partial x}+\alpha\left[\frac{\partial \Pi}{\partial y}\left(\frac{\partial u_1}{\partial y}+\frac{\partial v_1}{\partial x}\right)+2\frac{\partial \Pi}{\partial x}\frac{\partial u_1}{\partial x}\right. \tag{19}$$
$$\left.+\Pi\left(\frac{\partial^2 u_1}{\partial x^2}+\frac{\partial^2 u_1}{\partial y^2}\right)+U'\frac{\partial \pi_1}{\partial y}+U''\pi_1\right],$$
$$\frac{\partial v_1}{\partial t}+U\frac{\partial v_1}{\partial x}=-\frac{\partial \pi_1}{\partial y}+\alpha\left[\frac{\partial \Pi}{\partial x}\left(\frac{\partial u_1}{\partial y}+\frac{\partial v_1}{\partial x}\right)+2\frac{\partial \Pi}{\partial y}\frac{\partial v_1}{\partial y}\right. \tag{20}$$
$$\left.+\Pi\left(\frac{\partial^2 v_1}{\partial x^2}+\frac{\partial^2 v_1}{\partial y^2}\right)+U'\frac{\partial \pi_1}{\partial x}\right],$$
$$\frac{\partial u_1}{\partial x}+\frac{\partial v_1}{\partial y}=0\,. \tag{21}$$

Note that unlike in NF Poiseuille–Couette flows, in the present problem the basic flow pressure is a non-trivial function of both x and y coordinates which is written as $\Pi(x,y)=C_2(y)e^{C_0x/2}$, $C_2(0)=1$, see equations (9) and (12). For small values of C_0 the term $e^{C_0x/2}$ remains nearly constant for a relatively large range of x in the vicinity of some reference point x_0 so that we write approximately

$$\Pi(x_0,y)\approx C_2(y)E_0\,,\quad \frac{\partial \Pi}{\partial x}(x_0,y)\approx C_2(y)\frac{C_0}{2}E_0\,,\quad \frac{\partial \Pi}{\partial y}(x_0,y)\approx C_2'(y)E_0\,, \tag{22}$$

where $E_0=e^{C_0x_0/2}$. For negative values of C_0 and positive values of x which are of interest in the current study the range of values $1\geq E_0\geq 0$ corresponds to spatial locations ranging from the channel entrance to its exit which may be asymptotically far away from the entrance. Such an approximation significantly simplifies the subsequent analysis without sacrificing too much accuracy for small $|C_0|$.

Parametrisation (22) enables application of a standard normal mode expansion procedure where we assume the perturbation quantities in the form

$$(u_1(x,y,t),v_1(x,y,t),\pi_1(x,y,t))=(u_1(y),v_1(y),\pi_1(y))e^{(i\beta x+\sigma t)}\,. \tag{23}$$

This representation remains locally valid as long as the perturbation wavenumber

$$\beta\gg|C_0|/2\,. \tag{24}$$

We will show in Section 5 that this condition is safely satisfied for all considered regimes. In transformation (23), $\sigma=\sigma^R+i\sigma^I$ is the complex amplification rate with σ^I being the frequency of oscillations. The basic flow is linearly stable if $\sigma^R<0$.

Upon transformation (23) the perturbation equations (19)–(21) parameterised with E_0 become

$$\sigma u_1 = \left\{-i\beta U + \alpha E_0 \left[\beta C_2 (iC_0 - \beta) + (C_2' D + C_2 D^2)\right]\right\} u_1$$
$$- \left\{U' - i\beta\alpha E_0 C_2'\right\} v_1 - \left\{i\beta - \alpha \left[U'' + U' D\right]\right\} \pi_1 \,, \tag{25}$$
$$\sigma v_1 = \frac{1}{2}\alpha C_2 C_0 E_0 u_1' + \left\{i\alpha\beta U' - D\right\} \pi_1$$
$$- \left\{i\beta U - \alpha E_0 \left[\beta C_2 \left(\frac{i}{2} C_0 - \beta\right) + 2C_2' D + C_2 D^2\right]\right\} v_1 \,, \tag{26}$$
$$0 = i\beta u_1 + v_1' \,, \tag{27}$$

where both $'$ and D denote derivatives with respect to y.

5 Numerical results

We discretise the disturbance equations (25)–(27) using a pseudo-spectral Chebyshev collocation method of [20] and [21]. The advantage of this method is that it converges exponentially quickly: 100 collocation point was used to guarantee the accuracy exceeding 1% for all reported results.

Upon discretisation equations (25)–(27) result in a generalised algebraic eigenvalue problem for the complex amplification rate σ

$$(\mathbf{A} - \sigma\mathbf{B})\mathbf{X} = \mathbf{0}, \tag{28}$$

where $\mathbf{A} = \mathbf{A}(C_0, V, E_0, \alpha, \beta)$ and $\mathbf{B}$ are matrix operators resulting from the right- and left-hand sides of equations (25)–(27), respectively, and $\mathbf{X}$ is the eigenvector consisting of disturbance velocity components and pressure $(u_1, v_1, \pi_1)^T$.

Eigenvalue problem (28) was solved using an IMSL [22] routine DGVLCG for fixed values of C_0, V, E_0 and α (or, equivalently, Re^*) and over a range of wavenumbers β to determine the maximum of the amplification rate $\sigma^R_{\max} = \sigma^R(\beta_{\max})$, see Figure 1. While the value of $\beta_{\max}$ depends on the physical parameters of the problem the qualitative behaviour of the amplification rate curves remains the same in all investigated regimes. In all cases the instability (i.e. $\sigma^R_{\max} > 0$) was detected for one mode with a single maximum $\sigma^R_{\max}$ (refer to the top curves in Figure 1(a)–(d). The physical mechanism of this instability will be discussed in Section 5.2. The critical value of α (or Re^*) was subsequently determined by varying it iteratively for fixed values of other governing parameters until the condition $\left|\sigma^R_{\max}\right| \leq 10^{-7}$ was satisfied.

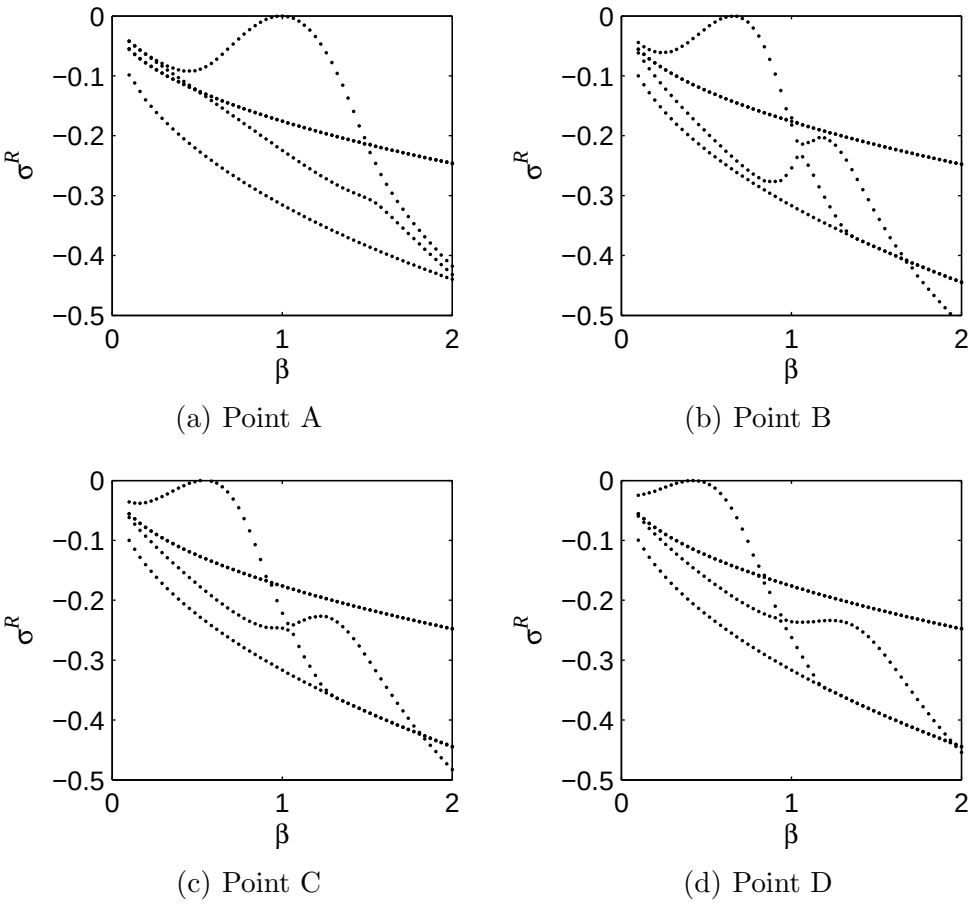

(a) Point A (b) Point B

(c) Point C (d) Point D

Fig. 1. Disturbance temporal amplification rates σ^R for four leading instability modes as a function of wavenumber β at points A–D in Figure 4 for $C_0 = -10^{-2}$ and $E_0 = 1$.

5.1 Critical parameters at the onset of instability

We discuss the case of small longitudinal pressure gradient $|C_0| \to 0$ first. In this limit PVF and NF flows become identical. The critical values of the Reynolds number and wavenumber obtained for both types of fluids for $C_0 = -10^{-4}$ are essentially the same. This classical case was considered in literature in the past [15–17]. It provides an accuracy check for our numerical algorithm. As seen from equation (15) in the limit $V \to 0$ the PVF flow reduces to NF Poiseuille flow. Thus we recover the well-known critical values for such a flow: $(Re^*, \beta) = (5772.22, 1.02)$ [23]. When $V \neq 0$, similarly to the analysis reported in [15–17] for plane NF Poiseuille–Couette flow, we find that as the wall velocity becomes larger, the value of the critical Reynolds number increases reaching a local maximum, then slightly decreases before rapidly increasing again without bound, see Figure 2(a). It is found that, like NF flows, Couette-type PVF flows satisfying the condition $U'(y) > 0$, $-1 \leq y \leq 1$ are always stable. The value of the critical wavenumber rapidly decreases with

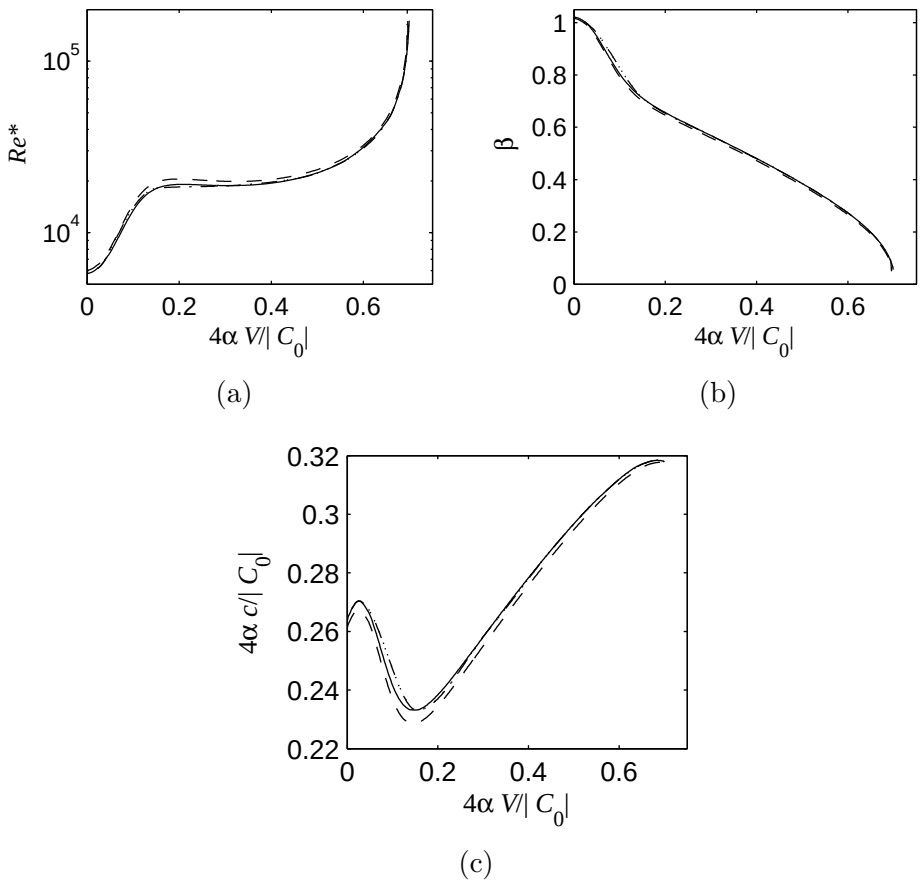

Fig. 2. (a) The critical Reynolds number Re^*, (b) wavenumber β and (c) scaled wavespeed $4\alpha c/|C_0|$ as functions of the scaled boundary velocity $4\alpha V/|C_0|$ for $E_0 = 1$ and $C_0 = -10^{-4}$ (dash-dotted lines) and $C_0 = -10^{-2}$ (NF—solid lines, PVF—dashed lines). The flow is unstable for $Re > Re^*$.

the wall velocity, see Figure 2(b) which is an intuitively clear result: a moving wall effectively stretches the instability structures which will be discussed in more detail in Section 5.2.

Figure 2(c) presents the ratio of the wavespeed $c = -\sigma^I/\beta$ of the most amplified disturbance mode and the maximum velocity of the Poiseuille flow component $|C_0|/(4\alpha)$ as a function of the scaled wall velocity $4\alpha V/|C_0|$. The behaviour of the critical wavespeed is non-monotonic. For small increasing wall velocities it also increases (the instability structures are slightly accelerated by the moving wall), but then the wavespeed starts decreasing relative to the wall velocity. As will be discussed in Section 5.2 this is due to the relocation of the critical layer where the condition $c = U$ is satisfied and the major disturbance production occurs [19] towards the stationary wall. For sufficiently large wall velocities the scaled disturbance wave speed starts increasing until it reaches its asymptotic value just below 0.32. It remains smaller than the wall velocity so that the critical layer only exists near the stationary wall when the ratio of

the wall velocity and the maximum Poiseuille component exceeds the value of about 0.245.

For larger pressure gradients the qualitative behaviour of the critical parameters remains the same, but a quantitative difference between the NF and PVF critical values of Reynolds number and wavespeed appears, compare the solid and dashed lines in Figure 2(a and c). PVF flows become more stable and the corresponding disturbance waves propagate slower than their NF counterparts. This is an anticipated result. Indeed the comparison of expressions (15) and (17) for PVF and NF velocities piezo-viscous effects lead to the reduction of the maximum flow velocity and, subsequently, the velocity gradients which are responsible for instability. At the same time the critical values of the wavenumber remain very close (lines in Figure 2(b) almost overlap). Overall, for both NF and PVF flows strengthening the Poiseuille component plays a destabilising role and leads to the increase of the disturbance wavenumber, while increasing the Couette component has the directly opposite effect. Our numerical results show that for both NF and PVF flows an instability does not occur if the ratio of the wall and Poiseuille velocities exceeds the value of $4\alpha V/|C_0| \approx 0.704$ which is in excellent agreement with the conclusion made in [15].

Despite this similarity between NF and PVF flows discussed above Figures 3 and 4 reveal two features which distinguish them drastically. Firstly, and somewhat counter-intuitively, increasing the pressure gradient parameter $|C_0|$ along the channel leads to significant flow stabilisation which is demonstrated for pure Poiseuille PVF flow in Figure 3(a) (see also [24]). This stabilisation is accompanied by a slight elongation of the instability structures as seen from the wavenumber data presented in Figure 3(b) and by the wavespeed decrease seen in Figure 3(c). Comparison of the solid and dash-dotted lines in Figure 4(a) also shows the stabilisation of Poiseuille–Couette flows for larger $|C_0|$. One reason for such a stabilisation is that as $|C_0|$ increases the PVF basic flow velocity profile discussed in detail in [2] straightens near the channel walls. In other words when the pressure gradient is increased the flow profile near the walls approaches that of Couette flow which is found to be stable. The second reason for stabilisation of PVF flows becomes evident from Figure 3(c): the critical wavespeed decreases when $|C_0|$ increases and therefore the critical disturbance production layer $c = U$ mentioned previously moves closer to the walls at which the disturbances are suppressed by the no-slip/no-penetration boundary conditions. It is also seen from Figure 3 that these piezo-viscous effects become noticeable for $|C_0| \gtrsim 10^{-2}$. For smaller pressure gradients PVF flows behave very similarly to ordinary fluid flows with constant viscosity.

Although the fluid considered here is assumed to have a shear-independent rheology the stabilisation of PVF Poiseuille-type flows in comparison with their NF counterparts is somewhat similar to that observed in shear-thickening flu-

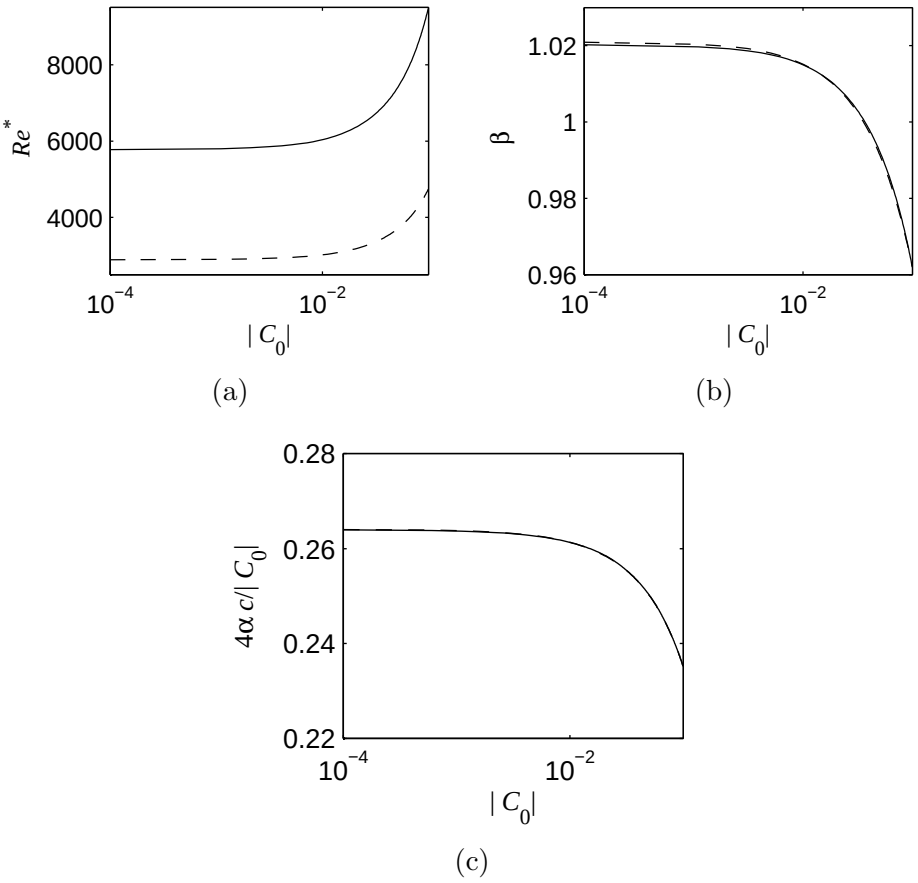

Fig. 3. (a) The critical Reynolds number Re^*, (b) wavenumber β and (c) scaled wavespeed $4\alpha c/|C_0|$ for plane Poiseuille flow ($V = 0$) as functions of the pressure gradient parameter C_0 for $E_0 = 1$ (solid lines) and $E_0 = 0.5$ (dashed lines). The flow is unstable for $Re > Re^*$. Solid and dashed lines overlap in plot (c).

ids. As follows from equation (12) the pressure distribution across the channel is such that it increases towards the walls (see also Figures 7–9(a) in Section 5.2). According to (4) this leads to the viscosity increase in the near-wall high-shear regions where instability is produced. The associated increase in viscous dissipation suppresses arising disturbances similarly to what happens in shear-thickening fluids even though such an effect is due to a larger viscosity and not due to a stronger shear.

The second feature which distinguishes NF and PVF flows is that the latter destabilise along the channel as the downstream coordinate x increases (or, equivalently, parameter E_0 decreases), compare the solid and dashed lines in Figures 3(a) and 4(a) for $C_0 = -10^{-4}$ and the dash-dotted and dotted lines lines for $C_0 = -10^{-2}$ in Figure 4(a). The reason for such a behaviour is traced back to the fact that the fluid viscosity is a linear function of pressure. Since according to equation (12) the pressure decreases along the channel, so does the fluid viscosity. The respective reduction in viscous dissipation encourages

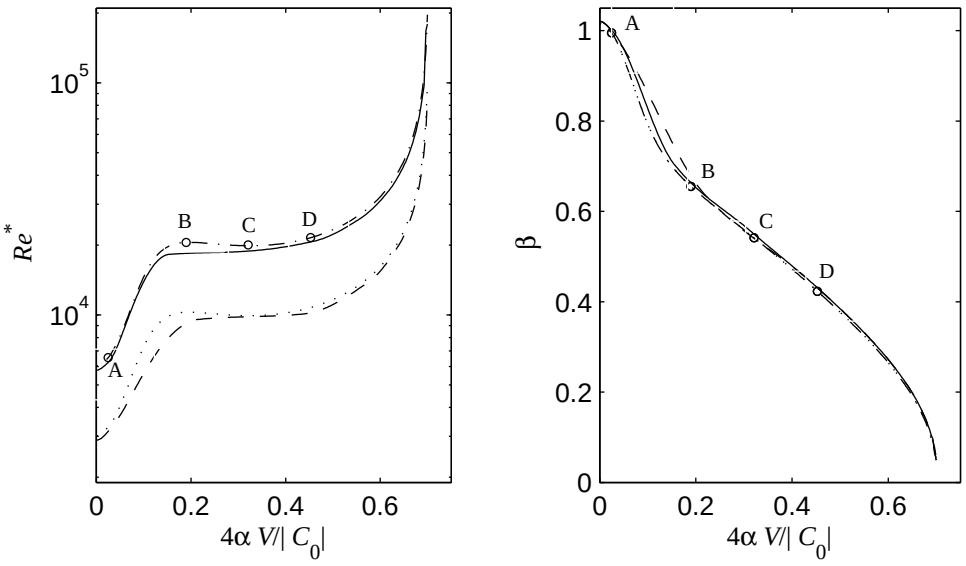

(a) (b)

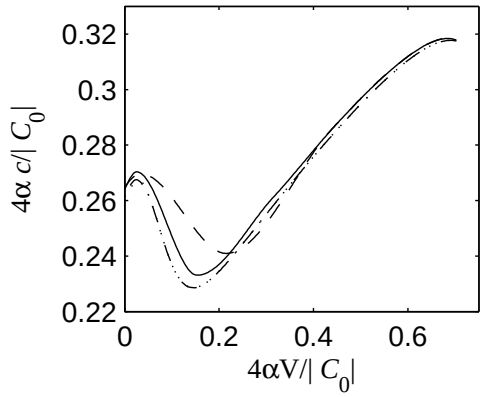

(c)

Fig. 4. (a) The critical Reynolds number Re^*, (b) wavenumber β and (c) scaled wavespeed $4\alpha c/|C_0|$ as functions of the scaled boundary velocity $4\alpha V/|C_0|$ for $C_0 = -10^{-4}$ (solid and dashed lines), $C_0 = -10^{-2}$ (dash-dotted and dotted lines) and $E_0 = 1$ (solid and dash-dotted lines) and $E_0 = 0.5$ (dashed and dotted lines). The flow is unstable for $Re > Re^*$. The dotted and dash-dotted lines overlap in plots (b) and (c).

the development of instability at the downstream locations at lower values of Reynolds number. Figure 5 confirms this. It shows that the decrease of the critical Reynolds number associated with the reduction of viscosity along the channel is essentially linear in E_0 (i.e. exponential in x) for pure Poiseuille flow ($V = 0$) for both $C_0 = -10^{-4}$ and $C_0 = -10^{-2}$, see the solid lines in Figure 5(a) and (b). In the limit of an infinitely long channel (i.e. for $E_0 \to 0$) PVF Poiseuille flow is inherently unstable because the critical $Re^* \to 0$. This means that no matter how small the actual flow Reynolds number is, PVF

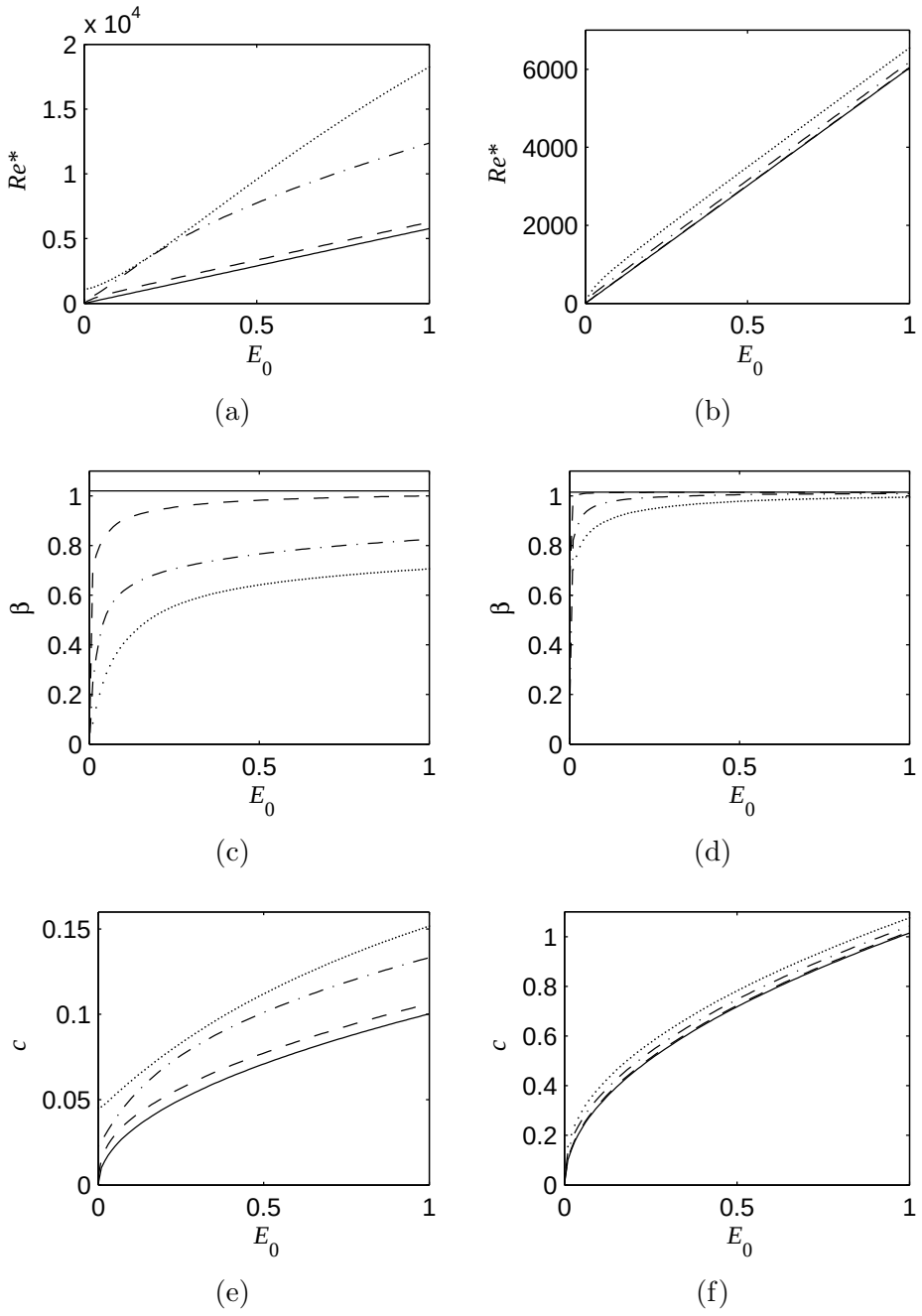

Fig. 5. (a) and (b) Critical Reynolds number Re^*, (c) and (d) wavenumber β and (e) and (f) wavespeed c as functions of E_0 defined in equation (22) for $C_0 = -10^{-4}$ ((a), (c), (e)) and $C_0 = -10^{-2}$ ((b), (d), (f)) and $V = 0$ (solid lines), $V = 0.01$ (dashed lines), $V = 0.05$ (dash-dotted lines), $V = 0.1$ (dotted lines).

Poiseuille flow will become unstable and will eventually break down far enough from the entrance to the channel. This is a remarkable distinction from NF Poiseuille flow which remains stable regardless of the length of the channel provided the flow is sufficiently slow at the channel entrance. However in drawing such a conclusion care should be taken since if the pressure along

Table 1
Critical values of the Reynolds number in the limit of very long channel ($E_0 = 10^{-4}$) for $C_0 = -10^{-4}$ and $C_0 = -10^{-2}$.

	$C_0 = -10^{-4}$				$C_0 = -10^{-2}$			
V	$\frac{4\alpha}{\lvert C_0\rvert}V$	$\frac{4\alpha}{\lvert C_0\rvert}c$	Re^*	β	$\frac{4\alpha}{\lvert C_0\rvert}V$	$\frac{4\alpha}{\lvert C_0\rvert}c$	Re^*	β
0	0	0.2638	0.6	1.020	0	0.2613	0.6	1.015
0.01	0.695	0.3182	11.2	0.084	0.148	0.2286	2.0	0.703
0.05	0.703	0.3176	273.1	3.5×10^{-3}	0.613	0.3122	3.5	0.247
0.1	0.704	0.3174	1091.6	8.9×10^{-4}	0.693	0.3175	11.2	0.084

the channel becomes too small the rheological model (4) is unlikely to remain valid [25].

As seen from Figure 5(a and b) parallel PVF Poiseille–Couette flow ($V \neq 0$) becomes more stable with increasing V at any location along the channel for the selected parameters. The critical value of the Reynolds number still decreases along the channel, but this decrease is not linear any more. More importantly, for $V \neq 0$ the limiting value of Re^* as $E_0 \to 0$ is not zero, see the dotted line for $V = 0.1$ in Figure 5(a) as well as data computed for $E_0 = 10^{-4}$ which is presented in Table 1. It increases with V. This means that for PVF Poiseuille–Couette flows there may exist a range of Reynolds numbers for which parallel basic flow remains stable even in very long channels. However this range is significantly narrower than that for conventional fluids with pressure-independent viscosity and it is further reduced as the applied pressure gradient increases, see Figure 5(b) and Table 1. This is consistent with our computational observations that PVF Couette-type flows with large wall velocity V remain stable. Note that in the limit $E_0 \to 0$ the wavenumber corresponding to the most dangerous disturbances tends to 0, see Figure 5(c) and (d), meaning that disturbance structures elongate down the channel to such a degree that they become effectively non-periodic and modify the mean flow. The data in Table 1 shows that despite the significant reduction of the critical wavenumber β the condition (24) is safely satisfied even for very small values of E_0 confirming the validity of parametrisation (22).

Figure 5(c–f) also shows that the elongation of the PVF flow disturbance structures in the downstream direction is accompanied by the decrease of their critical wavespeed for any fixed wall velocity. This is yet another feature distinguishing PVF flow from its NF counterpart for which the disturbance wavespeed remains constant along the channel. The wavespeed reduction is more pronounced for larger values of the pressure gradient parameter $|C_0|$.

5.2 Instability mechanism

To identify the physical mechanism of instability we consider the disturbance energy balance. We multiply the momentum equation (25) and (26) by the complex conjugate velocity components $\bar{u}_1$ and $\bar{v}_1$, respectively, add them together, integrate by parts across the layer and use the continuity condition (27) and boundary conditions $(u_1, v_1) = (\bar{u}_1, \bar{v}_1) = (0, 0)$ to obtain

$$\sigma^R \Sigma_k = \Sigma_{\alpha 1} + \Sigma_{\alpha 2} + \Sigma_{uv}\,, \tag{29}$$

where

$$\begin{aligned}
\Sigma_k &\equiv \int_{-1}^{1} E_k\, dy = \int_{-1}^{1} \left(|u_1|^2 + |v_1|^2\right)\, dy\,,\\
\Sigma_{\alpha 1} &\equiv \int_{-1}^{1} E_{\alpha 1}\, dy = -\alpha \int_{-1}^{1} \Pi \left[(|u_1'|^2 + |v_1'|^2) + \beta^2 \left(|u_1|^2 + |v_1|^2\right)\right]\, dy\\
&\quad +\alpha \int_{-1}^{1} \left[\frac{\partial \Pi}{\partial y} \Re\left(v_1 \bar{v}_1' + v_1' \bar{v}_1\right) - \frac{\partial \Pi}{\partial y \partial x} \Re(u_1 \bar{v}_1)\right]\, dy\,,\\
\Sigma_{\alpha 2} &\equiv \int_{-1}^{1} E_{\alpha 2}\, dy = \alpha \int_{-1}^{1} \left[U' \Re\left(\pi_1' \bar{u}_1 + i\beta \pi_1 \bar{v}_1\right) + U'' \Re(\pi_1 \bar{u}_1)\right]\, dy\,,\\
\Sigma_{uv} &\equiv \int_{-1}^{1} E_{uv}\, dy = -\int_{-1}^{1} U' \Re(v_1 \bar{u}_1)\, dy
\end{aligned}$$

and $\Re(\cdot)$ denotes the real part of the term in parentheses. The above terms have a straightforward physical meaning. Namely:

Σ_k represents the disturbance kinetic energy. Σ_k is positively defined. Therefore the sign of σ^R and therefore whether the flow is stable or unstable is determined by the sign of the sum of the three terms in the right-hand side of equation (29). Subsequently, the positive (negative) terms in the right-hand side play destabilising (stabilising) role.

$\Sigma_{\alpha 1}$ represents the viscous dissipation. The first integral in its definition is similar to that in pressure-independent Newtonian fluids and is negatively defined. The second integral takes into account the variation of a basic flow viscosity with pressure. The numerical contribution of the second integral is found to be small (it is proportional to C_0 and C_0^2, respectively) so that $\Sigma_{\alpha 1}$ remains negative signifying the stabilising role of the basic flow viscosity. Since within a linearised analysis framework the eigenfunctions (u_1, v_1, π_1) are defined up to a multiplicative constant we scale them in such a way that $\Sigma_{\alpha 1} = -1$ for all computed regimes.

$\Sigma_{\alpha 2}$ also represents the contribution to viscous dissipation however it is caused by the perturbation of viscosity due to the pressure disturbances. This term has no analogue in pressure-independent fluids and therefore it is instructive to consider it separately.

Table 2
Critical parameters and disturbance energy integrals for selected points in Figure 4 for $C_0 = -10^{-2}$ and $E_0 = 1$.

	V	$4\alpha V/\lvert C_0\rvert$	$\alpha \times 10^4$	Re^*	β	$4\alpha c/\lvert C_0\rvert$	$E_{\alpha 2}$	E_{uv}
A	0.1	0.0249	6.2170	6548	0.9952	0.2650	-0.1752	1.1752
B	1.3	0.1898	3.6500	20546	0.6554	0.2328	-0.2028	1.2028
C	2.1	0.3209	3.8208	19872	0.5416	0.2595	-0.1347	1.1347
D	3.0	0.4528	3.7732	21535	0.4231	0.2861	-0.0896	1.0896

Σ_{uv} represents the energy exchange between the basic and disturbance velocity fields.

Numerical results for selected marginal stability regimes for $C_0 = -10^{-2}$ and $E_0 = 1$ are presented in Table 2. They show that flow destabilization is always caused by the interaction between the disturbance and basic flow velocity fields. Namely, the velocity perturbations draw the energy from the basic flow so that $E_{uv} > 0$. At the same time term $E_{\alpha 2}$ remains negative. This means that piezo-viscous effects enhance viscous dissipation. In turn this leads to the increase of the critical Reynolds number for PVF observed in Figures 2(a) and 4(a). Note that the relative role of piezo-viscous dissipation is quite significant even for small values of C_0: it reaches 20% of the corresponding NF value for $C_0 = -10^{-2}$. The results for different values of C_0 and E_0 are found to be qualitatively similar and thus they are not discussed here.

In order to gain insight into the spatial structure of instability, in Figure 6 we present the distribution of disturbance energy integrands across the channel. The results show that for small wall velocities the disturbance energy production occurs in the narrow regions near the channel walls, see the dotted line in Figure 6(a). These correspond to a pair of classical Tollmien–Schlichting waves similar to those observed in pure Poiseuille NF flow, see, for example, [19]. They occur in the critical layers where the condition $c = U$ is satisfied. This is clearly seen from Figure 6(a and b): the horizontal solid lines show the locations of two critical layers near the walls which coincide exactly with the maximum of the disturbance energy production integrand E_{uv}. When the top wall velocity increases so that it exceeds the value of the critical wavespeed, see entries for points C and D in Table 2, only one Tollmien–Schlichting wave near the stationary wall survives while the disturbance energy production near the moving wall becomes negative. This means that the disturbance energy is fed back to the basic flow near the moving wall. As expected, the viscous dissipation integrand of $\Sigma_{\alpha 1}$ corresponding to the basic flow viscosity remains negative throughout the complete flow domain (see the solid lines in Figure 6). The strongest dissipation effects are observed very close to the channel walls which suppress velocity perturbations. This behaviour is typical for NF Poiseuille-type flows. However the distribution of the $\Sigma_{\alpha 2}$ integrand (see the

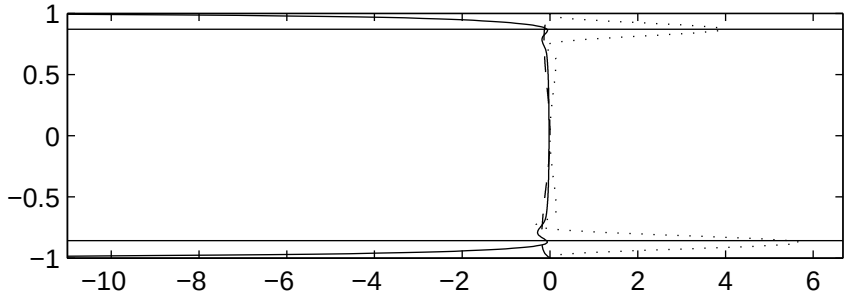

(a) Point A

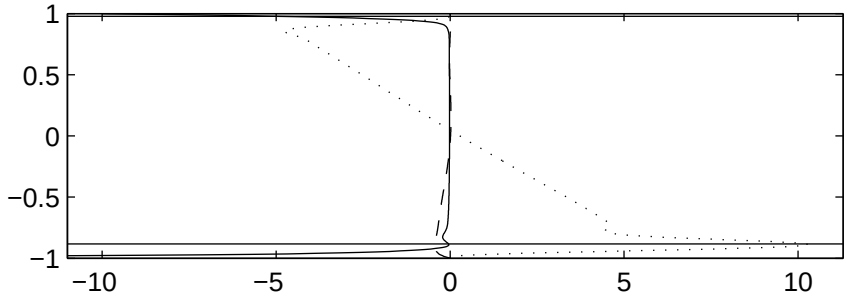

(b) Point B

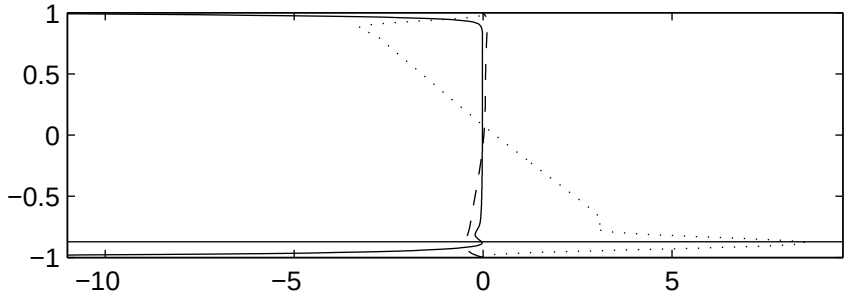

(c) Point C

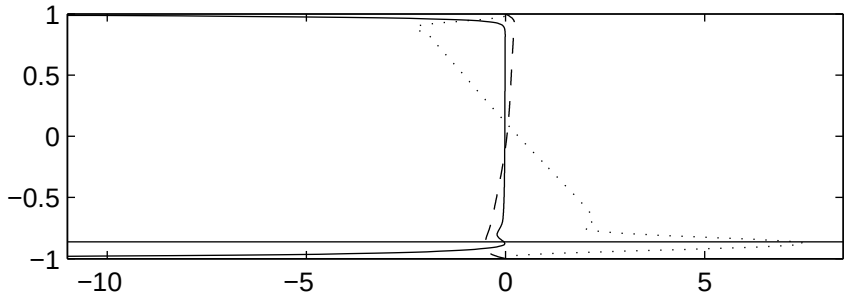

(d) Point D

Fig. 6. Disturbance energy integrands for points A–D in Figure 4. The solid, dashed and dotted lines correspond to the integrands of $E_{\alpha 1}$, $E_{\alpha 2}$ and E_{uv}, respectively. The horizontal solid lines indicate the location of the critical layer.

dashed lines in Figure 6) which represents piezo-viscous effects shows that it is only negative near the stationary wall, but becomes positive near the moving wall when its velocity is increased. Thus in contrast to their NF counterparts, in PVF flows piezo-viscous effects tend to make a flow near the moving wall less stable and a flow near the stationary wall more stable even though the overall effect of viscosity remains stabilising. The $\Sigma_{\alpha 2}$ data in Table 2 suggests that the overall piezo-viscous effects tend to become less stabilising as the wall velocity increases. This is indeed seen in Figure 4(a): as V becomes larger the curves for $C_0 = -10^{-2}$ approach those for $C_0 = -10^{-4}$ i.e. the NF limit.

In concluding this paper, in Figures 7–10 we present the basic flow velocity and pressure profiles and the most dangerous disturbance fields for selected points marked in Figure 4. For small wall velocities and $C_0 = -10^{-2}$ the basic flow velocity profile is close to parabolic and the basic flow pressure (and so the viscosity) is almost constant across the channel, see Figure 7(a). The instability pattern takes the form of two periodic sets of instability rolls located near the upper and lower walls shifted by a half of a wavelength with respect to each other, see Figure 7(b). As the upper wall velocity progressively increases two effects are observed as demonstrated in Figures 8–10(b). Firstly, the flow stabilises near the moving wall so that the top row of instability rolls seen in Figure 7(b) disappears in Figures 8–10. Secondly, the system of instability rolls near the bottom stationary wall survives, but the distance between the neighbouring rolls increases. Figures 8–10(b) also reveal a noteworthy correlation between the disturbance velocity and pressure fields for Poiseuille–Couette flows: the disturbance pressure achieves its maxima inside the vortices rotating counter-clockwise and minima inside the clockwise rotating vortices. Therefore the pressure is higher if disturbance vorticity has the sign opposite to that of the basic flow. The piezo-viscous fluid inside such vortices is slightly more viscous than inside the vortices rotating clockwise.

6 Conclusions

The stability of plane Poiseuille–Couette flows of a fluid whose viscosity increases linearly with pressure has been investigated. It was shown that in the limit of small longitudinal pressure gradients PVF flow solutions reduce to those for common NF fluids with constant viscosity. However for larger values of the pressure gradient PVF flows generally become more stable than their NF counterparts. Another significant distinction of PVF flows is that they tend to destabilise in the downstream direction even if they are stable in the vicinity of the channel entrance. The physical mechanism of instability is identified as Tollmien–Schlichting waves which appear in the critical layers near both channel walls when the upper wall velocity is small. When the wall velocity increases only one disturbance wave near the stationary

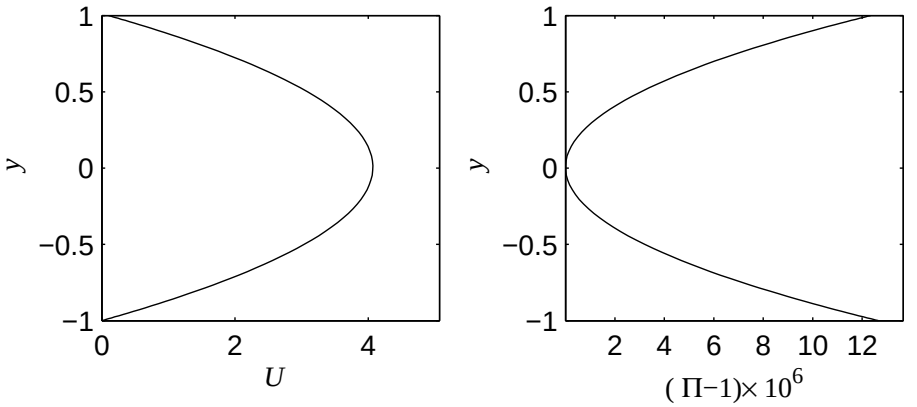

(a)

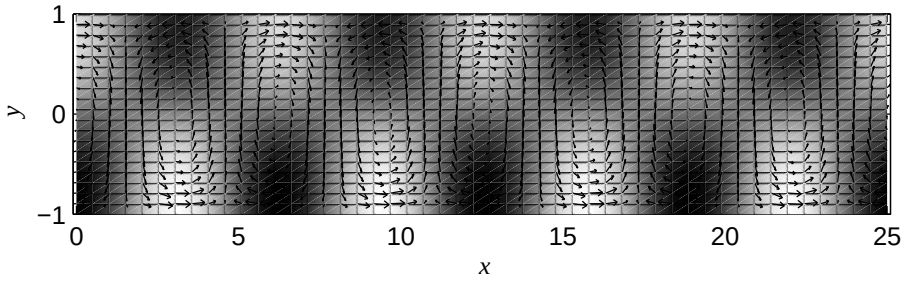

(b)

Fig. 7. (a) Basic flow velocity and pressure profiles and (b) disturbance velocity and pressure fields for point A in Figure 4. Lighter shading corresponds to higher pressure.

plate survives. It was also shown that the instability waves draw their energy from the basic velocity field and that the piezo-viscous effects play an overall stabilising role. Only stability of simple flows of shear-independent fluids has been considered in the current work. Analysis of shear-thinning or shear-thickening piezo-viscous fluids would proceed in a similar way and is planned to be presented elsewhere. However our preliminary results do not indicate that shear-thinning/thickening effects can lead to results qualitatively different from those presented here for shear-independent fluids.

References

[1] J. Hron, J. Málek, K. R. Rajagopal, Simple flows of fluids with pressure-dependent viscosities, Proc. R. Soc. Lond. A 457 (2001) 1603–1622.

[2] S. A. Suslov, T. D. Tran, Revisiting plane Couette-Poiseuille flows of a piezo-viscous fluid, J. Non-Newtonian Fluid Mech. 154 (2008) 170–178.

[3] F. Koran, J. M. Dealy, A high pressure sliding plate rheometry for polymer melts, J. Rheol. 43 (1999) 1279–1290.

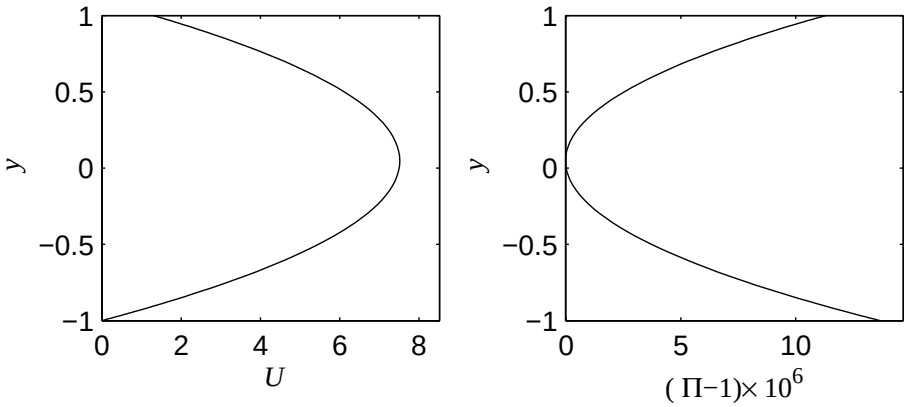

(a)

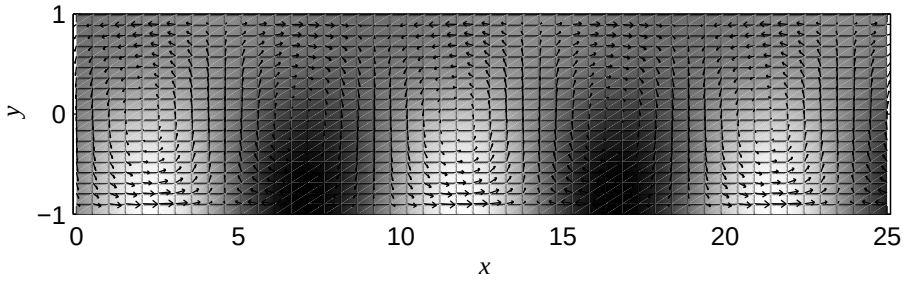

(b)

Fig. 8. Same as Figure 7 but for point B.

[4] T. W. Bates, J. A. Williamson, J. A. Spearot, C. K. Murphy, A correlation between engine oil rheology and oil film thickness in engine journal bearing, Society of Automotive Engineers (1986) 860376.

[5] D. R. Gwynllyw, A. R. Davies, T. N. Phillips, On the effects of a piezoviscous lubricant on the dynamics of a journal bearing, J. Rheol. 40 (1996) 1239–1266.

[6] M. Renardy, Some remark on the Navier-Stokes equations with a pressure-dependent viscosity, Comm. Partial Differential Equations 11 (1986) 779–793.

[7] F. Gazzola, A note on the evolution of Navier-Stokes equations with a pressure-dependent viscosity, Z. Angew. Math. Phys. 48 (1997) 760–773.

[8] G. Hay, M. E. Mackay, K. M. Awati, Y. Park, Pressure and temperature effects in slit rheometry, J. Rheol. 43 (1999) 1099–1116.

[9] J. Málek, J. Necas, K. R. Rajagopal, Global analysis of the flows of fluids with pressure-dependent viscosities, Arch. Rational Mech. Anal. 165 (2002) 243–269.

[10] J. Málek, J. Necas, K. R. Rajagopal, Global existence of solutions for flows of fluids with pressure and shear dependent viscosities, Appl. Math. Lett. 15 (2002) 961–967.

[11] J. Hron, J. Málek, J. Necas, K. R. Rajagopal, Numerical simulations and global existence of solutions of two-dimensional flows of fluids with pressure and shear dependent viscosities, Math. Comput. Simulations 61 (2003) 297–315.

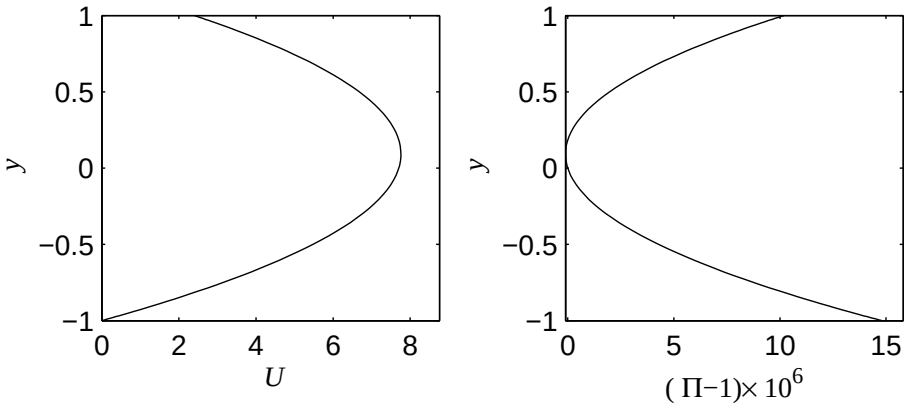

(a)

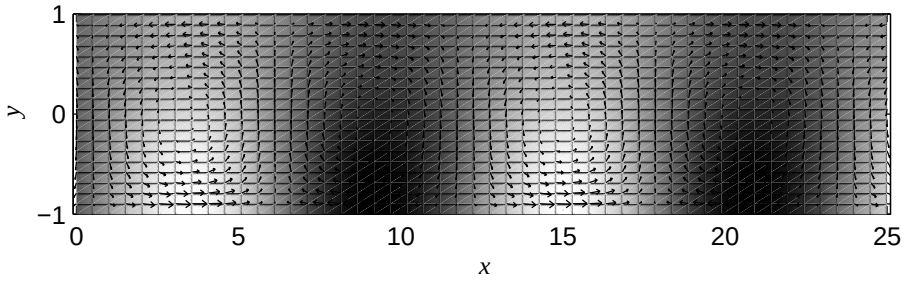

(b)

Fig. 9. Same as Figure 7 but for point C.

[12] M. Franta, J. Málek, K. R. Rajagopal, On steady flows of fluids with pressure- and shear-dependent viscosities, Proc. R. Soc. A 461 (2005) 651–670.

[13] K. R. Rajagopal, G. Saccomandi, Unsteady exact solution for flows of fluids with pressure-dependent viscosities, Math. Proc. R. Irish Academy 106A (2006) 115–130.

[14] M. Renardy, Parallel shear flows of fluids with a pressure-dependent viscosity, J. Non-Newtonian Fluid Mech. 114 (2003) 229–236.

[15] M. C. Potter, Stability of plane Couette-Poiseuille flow, J. Fluid Mech. 24 (1966) 609–619.

[16] W. C. Reynolds, M. C. Potter, Finite-amplitude instability of parallel shear flows, J. Fluid Mech. 27 (1967) 465–492.

[17] F. D. Hains, Stability of plane Couette-Poiseuille flow, The Phys. Fluids 10 (1967) 2079–2080.

[18] A. M. Sagalakov, The spectrum of small perturbations in plane Couette-Poiseuille flow, J. Appl. Mech. Tech. Phys. 2 (1971) 63–67.

[19] P. G. Drazin, W. H. Reid, Hydrodynamic Stability, Cambridge University Press, 1981.

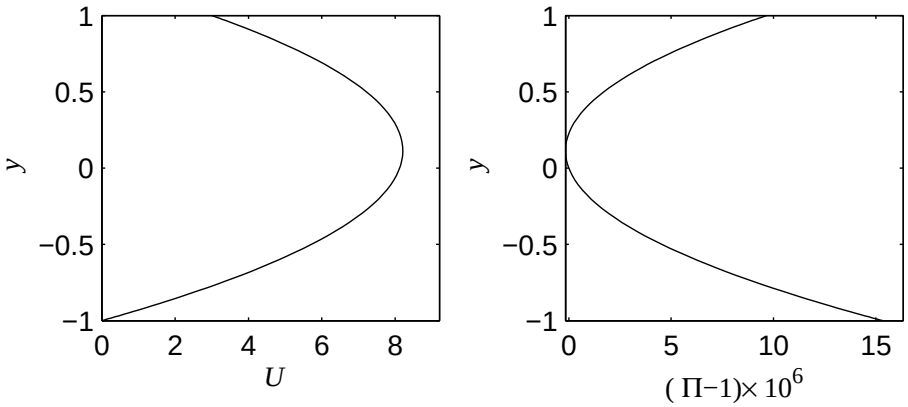

(a)

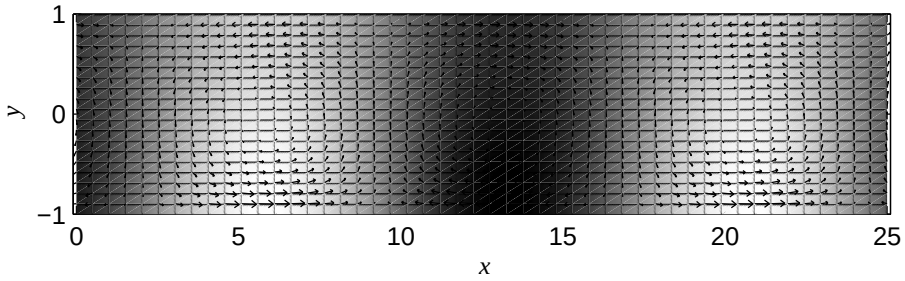

(b)

Fig. 10. Same as Figure 7 but for point D.

[20] H.-C. Ku, D. Hatziavramidis, Chebyshev expansion methods for the solution of the extended Graetz problem, J. Comput. Phys. 56 (1984) 495–512.

[21] D. Hatziavramidis, H.-C. Ku, An integral Chebyshev expansion method for boundary-value problems of O.D.E. type, Comp. & Maths with Appls 11 (6) (1985) 581–586.

[22] IMSL Inc., IMSL mathematical library, Tech. rep., Houston, TX (1995).

[23] S. A. Orszag, Accurate solution of the Orr-Sommerfeld stability equation, J. Fluid Mech. 50 (1971) 689–703.

[24] T. D. Tran, S. A. Suslov, Stability of plane Poiseuille flow of a fluid with pressure dependent viscosity, in: Proceedings of ICTAM08, International Congress on Theoretical and Applied Mechanics, Adelaide, Australia, ISBN 978-0-9805142-0-9, 2008.

[25] R. R. Huilgol, Z. You, On the importance of the pressure dependence of viscosity in steady non-isothermal shearing flows of compressible and incompressible fluids and in the isothermal fountain flow, J. Non-Newtonian Fluid Mech. 136 (2006) 106–117.